International Journal of Engineering Trends and Technology
ISSN: 2231–5381 / https://doi.org/10.14445/22315381/IJETT-V72I7P117

Volume 72 Issue 7, 157-167, July 2024

Original Article

Thermal Performance Enhancement of Parabolic Trough Collector: A New Generalized Correlation for the Optimum Diameter of the Absorber Tube

Anissa GHOMRASSI[1], Hatem MHIRI[2], Philippe BOURNOT[3]

[1, 2]*Thermal and Thermodynamics Laboratory in Industrial Processes, National Engineering School of Monastir, Tunisia.*
[3]*IUSTI, Marseille, France.*

[1]*Corresponding Author : ghomrassi.anissa@hotmail.com*

Received: 04 February 2024 Revised: 30 May 2024 Accepted: 15 June 2024 Published: 26 July 2024

Abstract - *The Parabolic Trough Solar Collector's (PTC) performance is enhanced by optimizing the absorber geometry. The proposed numerical method involves two essential steps. In the initial step, the Solar Heat Flux (SHF) focuses on a focal line, which is measured using Soltrace tools. The next phase involves optimizing the receiver's thermal performance with the use of Computational Fluid Dynamic (CFD) modelling. A sequence of numerical simulations is accomplished using Soltrace software and CFD code to investigate the impact of varying the receiver diameter. The numerical findings illustrate that the receiver diameter has a substantial impact on the performance of the PTC. Indeed, the results demonstrate that the increase in the receiver diameter improves the outlet temperature. However, it is undeniable that there exists an optimum receiver diameter beyond which the tube exit temperature decreases. As a result, a new correlation of the receiver tube's optimum diameter is consequently inferred to generalize this latter outcome. The correlation coefficient of determination (R^2) is 95.8%.*

Keywords - *Empirical correlation, FVM method, MCRT method, PTC, Receiver tube optimum diameter.*

1. Introduction

Future generations are expected to fulfil their mounting energy needs with solar energy, which is thought to be a clean, endless energy source. Due to its significant capacity and the imperative to reduce greenhouse gas emissions, solar energy is a top choice for advancement. With its abundance, it is compelling to harness solar energy through the use of reflectors to achieve the high temperatures necessary for electricity generation. The PTC is the most widely accepted technology for concentrating solar power due to its precision and cost-effectiveness in large-scale solar power production, outperforming other technologies like solar tower systems, Fresnel reflector mirrors, and solar dishes [1, 2]. The significance of the PTC has prompted researchers to investigate ways to enhance their performance through both experimental and numerical methods. Experimental measurement can be utilised to research the thermal and dynamic properties of PTC, but it is not capable of studying the optical characteristics of this system. Therefore, employing numerical studies can serve as a remedy to enhance its optical performance. The PTC is principally composed of an absorber, mirrors, and a support structure [3]. Because the absorber tube is the key component of the PTC, many bibliographic researches are contributing to enhancing its performance. To assess the optical efficiency of a solar energy conversion system, it is crucial to measure the concentrated SHF and determine how it is distributed over the lower half of the tube's circumference. It is worth noting that there are few bibliographic reviews dealing with the optical analysis of PTC systems that can be encountered in the literature. Notably, Jeter [4] is the only researcher to have determined the SHF distribution in the focal line of the PTC receiver. This author has developed a semi-finite analytical formulation for SHF. The optical efficiency of collectors is then estimated using the developed model. In Jeter's research papers [4, 5], the SHF in the PTC focal plane is presented and compared for various incidence angles and also for diverse PTC opening radii. More recently, Cheng et al. [6] carried out an optical study by the use of the Monte Carlo Ray Tracing Method (MCRT), in which they compared a few common PTC systems that are available. Furthermore, the study provides a thorough analysis of how key geometric parameters affect the overall properties and optical performance of PTC systems in a range of operating scenarios. The study shows that PTC systems with varied geometric characteristics display different levels of sensitivity to different types of optical defects under different operating situations. PTC absorbers were the subject of experimental thermal research by Dongqiang et al. [7]. The purpose of the tests was to look at heat losses and how tube coating affects emissivity. The experimental studies

undertaken by Dongqiang Lei et al. [7] made it possible to establish a correlation between absorber temperature and heat losses. The absorber has low emissivity, measuring less than 10% at 400° C, according to experimental results, which support the study's examination of the thermal insulation effect.

Because measuring experimental solar heat flux is so difficult, the focus of all prior experimental research has been on the absorber tube's thermal behaviour. Therefore, it becomes imperative to develop numerical methods to deeply focus on the optical behaviour of ray beams concerted on the receiver tube and quantify the SHF in the receiver tube periphery [24, 25]. Subsequently, we will elaborate on the main bibliographic reviews of proposed numerical works meant to enhance the PTC's system performance.

The MCRT is used to estimate the SHF on the absorber tube periphery. This method has been commonly used in past research on solar parabolic dishes and tower power plants. The validity of the MCRT method in estimating the SHF distribution is a crucial step in all numerical modelling. Consequently, evaluating the MCRT modelling method for solar conversion systems has been the primary focus of several studies [8, 9].

Their main objective was to ensure the capability of the MCRT model to offer accurate predictions of SHF on the receivers of tower power plants and solar parabolas. De la Torre et al. [10] introduced a thorough database detailing the MCRT method and its formulations related to every MCRT algorithm application for both solar energy conversion systems, including solar towers and Fresnel linear reflectors. Chen et al. [11] have considered the nature of the non-uniform SHF by combining also MCRT-FVM in order to study a PTC using a nanofluid absorber.

As previously indicated, most numerical studies of solar tower plants and also solar dish systems have employed Soltrace software based on the MCRT method. Nevertheless, there are limited bibliographic references studying PTC systems.

The MCRT is often coupled with Computational Fluid Dynamics (CFD) models to precisely replicate experimental findings and predict patterns of thermal and dynamic flow fields. Wang et al. [12, 13] were the first researchers to use a coupled analysis, combining MCRT and the FVM. For both concentric and eccentric absorbers, three-dimensional simulations were run in order to record the focused heat flux, temperature, and also thermal stress profiles.

Depending on the literature, many scientists fixated on ameliorating the PTC's effectiveness by varying a wide range of geometric characteristics. Therefore, the objective of this study is to discuss the PTC performance improvement by varying absorber tube diameter and by creating a novel correlation that had not previously been investigated. This correlation is capable of determining the optimum diameter of the PTC receiver. This finding could be truly useful in optimising the PTC system's performance.

2. Experimental Results

2.1. Experimental Setup

PTC was designed, fabricated, and tested experimentally in an arid climate Figure 1. The PTC is positioned in a southward direction and firstly tilted at an angle of 34° from the horizontal, which corresponds to the latitude of the testing location. It functions with a 0.2 Kg/s mass flow rate. Environmental conditions, including solar irradiance, wind speed, and also ambient temperature were measured and displayed in Figure 2. K-type thermocouples are used for temperature measurement. They have a sensitivity of 40µV/°C, and their accuracy is ±1.5°C within the specified range of -40°C to 380°C. A solarimeter is utilized to quantify solar radiation with ±2% relative precision and a sensitivity of 8 µV/Wm^{-2}. Windspeed is measured by an anemometer with ±0.2 m/s relative precision.

2.2. Experimental Performance Exploration

Throughout these trials, the highest level recorded of the incident solar irradiance was around 750 W/m^2. The higher average ambient temperature (T_a) reached a maximum of 42 °C, and these peaks occurred between 12:00 PM and 4:00 PM see Figure 2. This finding is a defining feature of the arid climate. Undoubtedly, T_a persists at a high level till 4:00 PM. Figure 2 depicts the distribution of wind speed.

Fig. 1 The designed PTC

The wind speed change is actually stochastic, exhibiting considerable strength in the morning and diminishing to a lower intensity in the afternoon. Glass envelope temperatures are also presented in Figure 2. This curve has a similar pattern as the ambient temperature evolution, but the temperature level attains a higher level. Figure 3 displays the both temperatures at which the working fluid enters and exits. The highest temperature recorded at the exit was 97 °C, and this value was reached during the time period from 12:00 PM to 2:00 PM.

Table 1. Experimental equipment

	Unit	Measure instruments	Models
Fluid Temperature	°C	A Fluke	Fluke 63
Solar Irradiation	W/m2	A digital Solarimeter	CR 100
Wind Speed	m/s	A Digital anemometer	Ms6252A

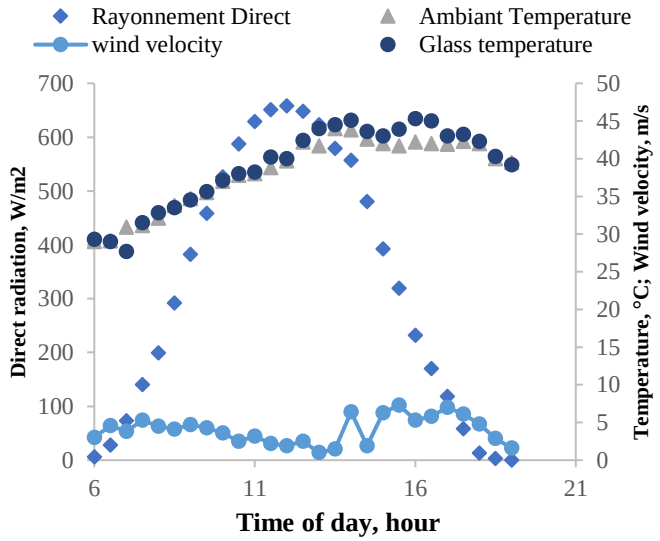

Fig. 2 Meteorological conditions measurements on july 4th

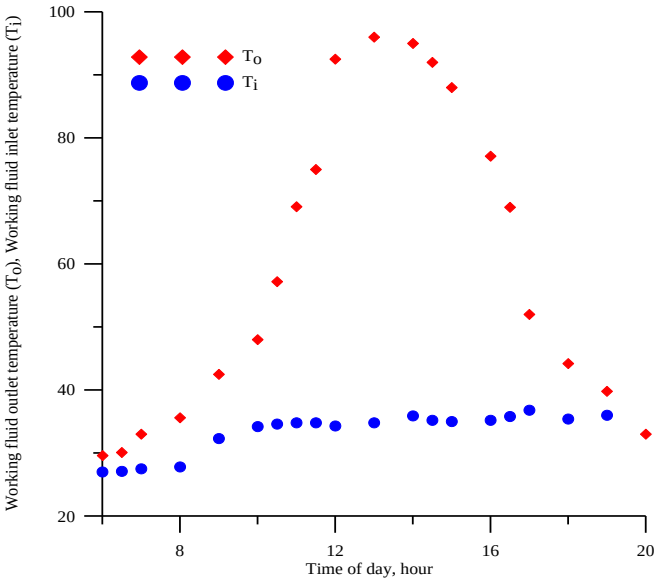

Fig. 3 Temperature variation of the working fluid on july 4th

2.3. PTC's Efficiency

In order to ensure the usability of results measured over the course of the year, the instantaneous efficiencies for the PTC manufactured and tested were calculated. The efficiency climb is shown in Figure 4.

Multiple experimental tests were performed to assess the PTC's thermal efficiencies using a constant operating fluid flow rate of 0.2 kg/s. The PTC thermal efficiencies (η) under the given operational parameters as a function of $\frac{T_i-T_a}{G}$ are represented in Figure 6. The graph illustrates that the instantaneous efficiency exhibits a linear function of $\frac{T_i-T_a}{G}$ and can be mathematically represented by Equation 1.

$$\eta = 0.45825 - 0.6484\left(\frac{T_i-T_a}{G}\right) \quad (1)$$

Nevertheless, the thermal efficiency of this specific device is typically determined and calculated using the subsequent mathematical statement (Equation 2) [14]:

$$\eta = F_R\eta_0 - \frac{F_R U_L}{CR}\frac{T_i-T_a}{G} \quad (2)$$

With: $\eta_o = \rho.\ \tau.\ \alpha\ \gamma = 0{,}6$

CR represents the concentration rate, which is defined as:

$$CR = \frac{A_a}{A_r} \quad (3)$$

By utilizing Equations (2) and (3), the slope and the intercept factor provide the necessary information to calculate the PTC's total loss coefficient (U_L) and the conductance factor (F_R). Therefore, it can be inferred that U_L = 85,05W/m²K and F_R = 0,77. The conductance factor exhibits competitiveness in comparison to the PTC systems mentioned and referenced in the literature [14, 15, 11]. These results are interesting because they can be used all year round.

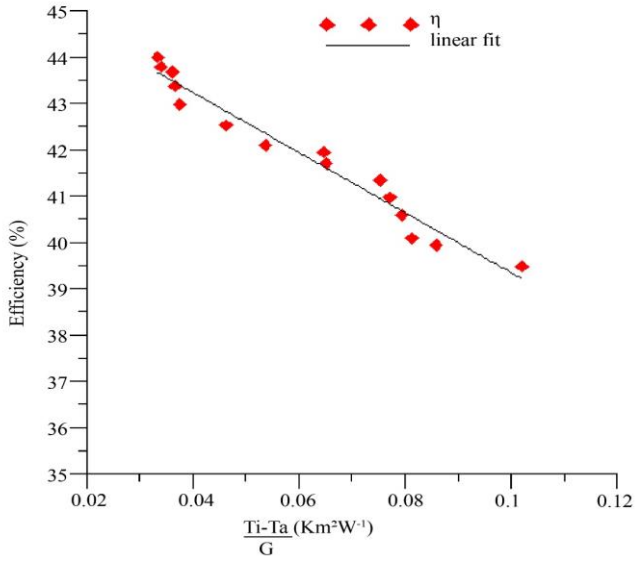

Fig. 4 The progressions of thermal efficiencies

Table 2. PTC Geometrical and optical utilized in this investigation

PTC system	Value (m)		Receiver	Glass tube	Reflector mirrors
W_a	1	**Absorptivity**	0.95	0.01	0
f	2				
L	2	**Reflectivity**	0	0.01	0.9
d_{ri}	0,06				
d_{ro}	0,07	**Transmissivity**	0	0.965	0.05
d_{gi}	0,1	**Slope error (mrad)**	0.0001	0.0001	3
d_{go}	0,105	**Specularity error (mrad)**	0.0001	0.0001	0.3
φ	45°				

3. Numerical analysis

3.1. Parameters of the PTC

The PTC consists of two fundamental elements: a reflector made of silver-coated glass mirrors and a stainless-steel receiver tube. Concentrators reflect direct irradiation and concentrate it on an absorber in the focal line (refer to Figures 5 and 6). A glass envelope encloses the receiver. The metallic tube is painted with a selective coating to increase absorptivity and minimise emissivity. The glass envelope is used to minimise heat losses. The PTC system's geometric specifications are provided in Table 2. The analysis of the PTC's performance entails two primary methods. Firstly, the Soltrace software [16] is employed to calculate the distribution of SHF within the focus zone of the PTC. Additionally, the thermal performance of the absorber is examined and enhanced using the industrial software ANSYS [17]. Soltrace software uses the ray-tracing method (MCRT) to predict concentrated heat flux, which serves as the boundary conditions for the outer periphery of the receiver tube.

3.2. Optical Analysis

3.2.1. Ray Tracing

The MCRT method was executed via an optical modelling programme, Soltrace. Within this research investigation, The SHF calculations were estimated for June 21 at 12:00 local time (latitude: 39.5, longitude: 116.2, DNI: 1000 W/m^2). The "Pillbox" approximation was selected to represent the form of the sun with a half-width of σ= 4.65 mrad as described by Sargent and Lundy [18]. In Table 2, we specified the optical properties of each PTC component. The reflectivity glass envelope was set to zero, while transmissivity values were taken at 0,965. The absorber exhibits a null transmissivity, a reflectivity of 0,04, the absorptivity was 0,95 and optical errors were set to zero. A reflectivity value of 0,9 was assigned for mirrors, and the transmissivity was set to zero, as indicated in Table 2.

3.2.2. SHF Distribution Across Absorber Tube

We obtained the SHF's distribution on the receiver tube upon initiating the calculation operation. The determined SHF exhibits a pronounced spike distribution, as depicted in Figure 7. The curve is partitioned into four sections, described as follows: The SHF is very small during the first part, as the absorber tube gets only direct radiation emitted from the glass envelope. However, in the second part (part II), the SHF rises quickly and reaches a peak of 45200W/m^2. The concentration of SHF reaching the absorber tube's lower periphery is rapidly increasing. The SHF intensity rapidly diminishes in the third part (part III) as the reflected rays diminish. A small quantity of rays distinguishes the final part arriving at the receiver tube's outer edge. This part is characterized by a very low SHF in this part Figure 7.

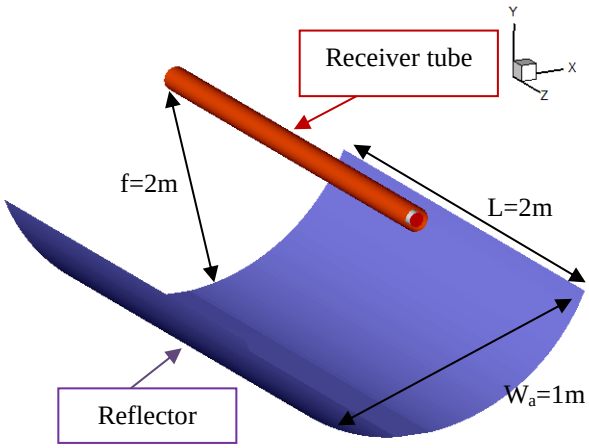

Fig. 5 PTC system studied details

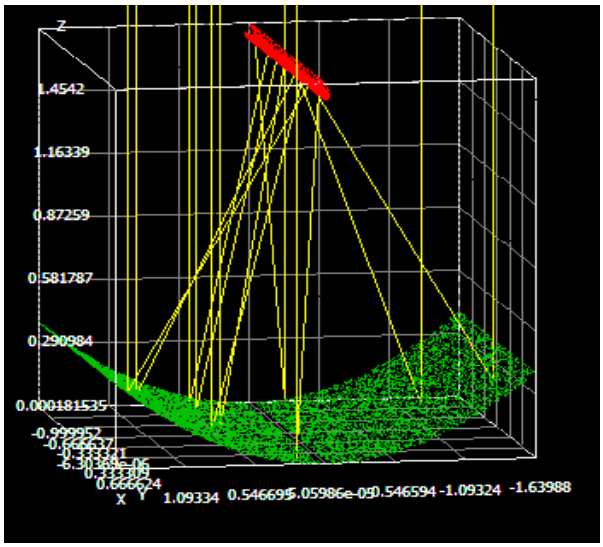

Fig. 6 Examples of several incident rays traced for a PTC system

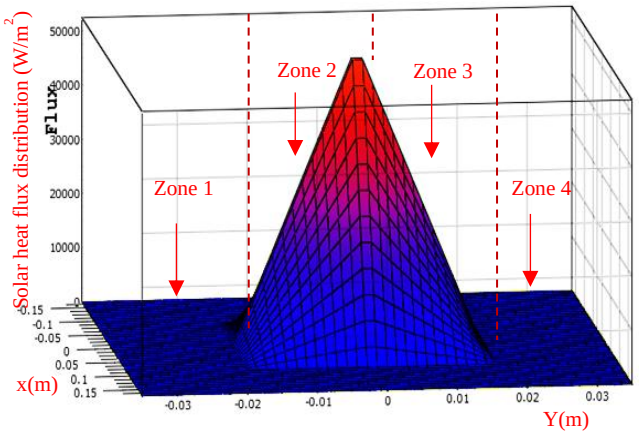

Fig. 7 The SHF distribution on the absorber tube periphery

3.3. Thermal Analysis

3.3.1. Assumptions

Since real conditions are frequently challenging to solve numerically, it is customary to incorporate simplifying hypotheses in order to clarify the studied situation. The assumptions adopted in this study are the following:

(a) Steady state
(b) Turbulent flow
(c) An incompressible fluid
(d) Mixed convection involves the use of Boussinesq approximations to consider the density variation that occurs with temperature variations:

$$(\rho - \rho_0) \approx -\rho_0 \beta (T - T_0) \quad (4)$$

Where ρ_0 represents the density at T_0

(e) The annular space is a state of vacuum.
(f) The absorber tube contains Syltherm 800 as an operating fluid.

In accordance with the methods described by Cheng et al. [6], the physical characteristics of this thermal oil vary with temperature and are represented by polynomial equations. The polynomial functions are specified in Table 3.

3.3.2. Governing Equations

The SHF, determined using the MCRT described overhead, is implemented into the ANSYS software as thermal boundary conditions (User Defined Function: UDF) on half of the absorber's perimeter that is exposed to the mirror. Numerical analysis is used to study the dynamic and thermal characteristics of the working fluid in the absorber. The numerical calculations were conducted on an Intel Xeon 4 CPU running at a frequency of 3.6 GHz and equipped with 10 GB RAM. Every run necessitated around 8 days of real calculating time.

The governing conservation equations of continuity, momentum and energy are expressed as follows:

$$\frac{\partial(\rho\overline{u_i})}{\partial x_i} = 0 \quad (5)$$

$$\frac{\partial}{\partial x_j}\left(\rho\overline{u_\iota}\,\overline{u_j}\right) = -\frac{\partial \bar{P}}{\partial x_i} + \frac{\partial}{\partial x_j}\left[\mu\left(\frac{\partial \overline{u_i}}{\partial x_j} + \frac{\partial \overline{u_j}}{\partial x_i}\right) - \frac{2}{3}\mu\frac{\partial \overline{u_i}}{\partial x_i}\delta_{ij} - \rho\overline{u_i' u_j'}\right] \quad (6)$$

$$\frac{\partial}{\partial x_j}\left(\rho\overline{u_j}\,C_p\overline{T}\right) = \frac{\partial}{\partial x_j}\left(\lambda\frac{\partial \bar{T}}{\partial x_j} + \frac{\mu_t}{\sigma_{h,t}}\frac{\partial(C_p\bar{T})}{\partial x_j}\right) + \overline{u}_j\frac{\partial \bar{P}}{\partial x_j} + \left[\mu\left(\frac{\partial \overline{u_i}}{\partial x_j} + \frac{\partial \overline{u_j}}{\partial x_i}\right) - \frac{2}{3}\mu\frac{\partial \overline{u_i}}{\partial x_i}\delta_{ij} - \rho\overline{u_i' u_j'}\right]\frac{\partial \overline{u_i}}{\partial x_j} \quad (7)$$

The model of turbulence k-RNG represents a closed system of the previous equations.

The Transport equations for k and ε are written as follows:

$$\frac{\partial(\bar{\rho}\tilde{u}_i k)}{\partial x_i} = \frac{\partial}{\partial x_i}\left[\alpha_k \mu_{eff}\frac{\partial k}{\partial x_i}\right] + G_k + G_b - \bar{\rho}\varepsilon \quad (8)$$

$$\frac{\partial(\bar{\rho}\tilde{u}_i \varepsilon)}{\partial x_i} = \frac{\partial}{\partial x_i}\left[\alpha_\varepsilon \mu_{eff}\frac{\partial \varepsilon}{\partial x_i}\right] + C_{\varepsilon 1}\frac{\varepsilon}{k}(G_k + C_{\varepsilon 3}G_b) - C_{\varepsilon 2}\bar{\rho}\frac{\varepsilon^2}{k} - R \quad (9)$$

The model of turbulence k-ε RNG represents a closed system of previous equations. Table 4 presents a concise overview of the standard coefficients used in the k-ε RNG model. The radiation model applied is the Discrete Ordinates (DO) model. This model allows selective materials' introduction, also emission and absorption from one surface to another are wavelength-dependent.

The radiative transfer equation (ETR) is expressed as follows:

$$\frac{\partial G(\vec{r},\vec{s})}{\partial s} + (a+\sigma_s)G(\vec{r},\vec{s}) = an^2\frac{\sigma T^4}{\Pi} + \frac{\sigma_s}{4\Pi}\int_0^{4\Pi} G(\vec{r},\vec{s})\Phi\left(\vec{s},\vec{s}'\right)d\Omega' \quad (10)$$

Table 3. Physical properties of the syltherm 800

	a + b.T (K) + c.T² (K) + d. T³ (K) + e.T⁴ (K)				
	a	**b**	**c**	**d**	**e**
$\boldsymbol{\rho(kg\ m^{-3})}$	1.105702×10^{3}	-4.153495×10^{-1}	-6.061657×10^{-4}	0	0
$\boldsymbol{C_p(JK_g^{-1}K^{-1})}$	1.107798×10^{3}	1.708	0	0	0
$\boldsymbol{\lambda\,(Wm^{-1}K^{-1})}$	1.90021×10^{-1}	-1.875266×10^{-4}	$-5.753496 \times 10^{-10}$	0	0
$\boldsymbol{\mu\,(Pa\ s)}$	8.486612×10^{-2}	-5.541277×10^{-4}	1.388285×10^{-6}	1.566003×10^{-9}	6.672331×10^{-13}

Table 4. Typical values of k-ε RNG turbulence model constants

C_μ	$C_{\varepsilon 1}$	$C_{\varepsilon 2}$	$C_{\varepsilon 3}$	σ_k	σ_ε	η_0	β
0.0845	1.42	1.68	1	0.718	1.39	4.38	0.012

3.3.3. Boundary Conditions

The boundary conditions shown in Figure 2 are enumerated below:

- For receiver inlet: $\dot{m} = 0.374\ kg/s$ and $T = T_i = 300K$

- For receiver outlet: fully developed assumption $\frac{\partial u}{\partial x} = \frac{\partial v}{\partial x} = \frac{\partial w}{\partial x} = \frac{\partial k}{\partial x} = \frac{\partial \varepsilon}{\partial x} = \frac{\partial p}{\partial x} = 0$ and $\frac{L}{d_{ri}} = 33$

- The lateral side and glass envelop tube surfaces are classified as "Wall".

- We expect a "Mixed" heat transfer to occur between the exterior glass envelope wall and the surrounding environment. The ambient temperature (T_{amb}) combined with the outside radiation temperature (T_{sky}) are detailed in this case and related by the next equation [19]:

$$T_{sky} = 0.0552\ T_{amb}^{1.5} \quad (11)$$

According to S.C. Mullick et al. [23] and Cheng et al. [6], equation (12) represents the expression concerning the heat transfer coefficient (h_w) surrounding the envelope of glass:

$$h_w = 4v_w^{0.58} d_{go}^{-0.42} \quad (12)$$

- The bottom part of the absorber tube, facing the mirrors, is affected by a non-uniform SHF distribution. This distribution is computed using the Soltrace software (see Section 3.2.2).

- The upper half perimeter is subjected to an incident SHF equal to 1000W/m^2.

4. Optimization Results and Discussions

4.1. Numerical Modelling

Equations 5, 6, and 7 pertaining to their respective boundary conditions were solved by the Finite Volume approach (FVM) using ANSYS. Before that, Gambit, an ANSYS pre-processor, was utilised to generate a geometry that was meshed with quadrilateral cells. A non-uniform grid arrangement was used to discretize the computing domain. The mesh has a higher level of refinement in each of the angular and radial planes, as well as in close proximity to walls. A total number of 765440 nodes were utilised for the numerical simulations Figure 8 The model of k-ε RNG, in conjunction with a model that accounts for the effects near the wall (Enhanced Wall Treatment) suggested by Dongqiang et al. [7] and Kalogirou [20], is used as the closure model.

We have chosen to use the first-order Upwind scheme for all equations, with the exception of momentum and energy, where it is preferable to employ the scheme of second-order Upwind [13, 21]. A simple algorithm is employed to accomplish the coupling between pressure and velocity. The Discrete Ordinate model (DO) was chosen to consider the radiative transmission between the external wall of the absorber tube and the inside surface of the glass envelope. This model enables radiation computation in semi-transparent zones, such as glass, and enables radiative exchanges between non-grey surfaces. The DO model is distinguished by using angular discretization in spatial representation for two spectral bands. The convergence criteria were defined to be less than 10^{-5}, except for energy and DO, which was less than10^{-7}.

4.2. Receiver Tube Heat Transfer Analysis

When the sun is shining, mirrors reflect the energy from the sun and focus it onto the HCE. A portion of this energy is captured via the glass envelope, while the remaining portion is transmitted and captured by the receiver's selective coating. Only a fraction of the energy that is absorbed is transported for the HTF through forced convection, while another portion is sent back to the glass envelop through natural convection and also thermal radiation. The heat derived via the absorber, through convection and thermal radiation, traverses the glass enclosure and is subsequently released into the surrounding environment.

4.2.1. Thermal Analysis

A precise schematic depiction of the receiver is presented in Figure 9. The receiver consists primarily of an interior absorber tube coated by a particular outer layer, an outside glass envelope, and an annular space under vacuum maintained at a low pressure of 0.0001 Torr. An exhaustive analysis of a PTC's receiver using 3D-CFD should incorporate the following heat transfer mechanisms illustrated in both Figures 9 (a- b). Heat transfer Radiation occurs due to the temperature variation between the outside surface and the sky.

The overall modelling approach relies on an energy balance calculation around the Heat Collector Element (HCE). It encompasses direct sunlight, which is received, the optical losses caused by both the concentrator and the HCE, heat losses from the HCE, and the heat gained in HTF. To determine the analytical expression for the absorber's optimal diameter, an energy balance must be applied to the absorber tube's external surface. This heat transmission model applies an energy balance to analyse the heat distribution within each component of the HCE. The integral form of the energy equation states that the useful heat generated by a solar collector is identique to the energy absorbed by the fluid used for heat transfer, minus heat losses occurring either directly or indirectly from its surface to the environment.

Temperatures and SHF exhibit variations throughout the circumference of the heat-collecting element, except for the fluid, which only fluctuates along the absorber's length. Therefore, a heat transfer balance is implemented in each control volume. The temperature gradient within the heated working fluid and the surrounding atmosphere leads to heat being lost through the absorber to the glass envelope as well as from the glass enclosure onto the atmosphere.

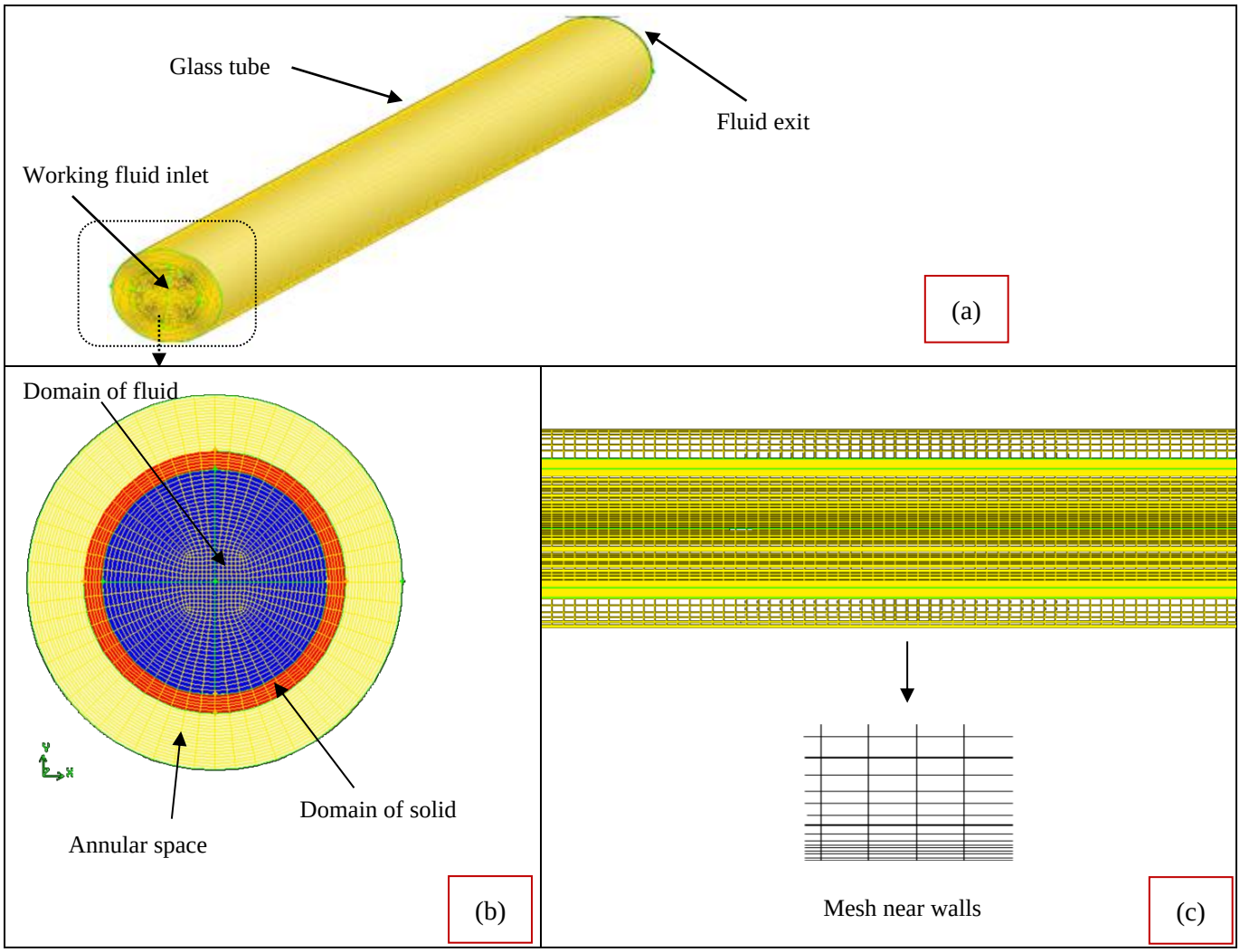

Fig. 8 (a) Longitudinal mesh (b) Cross section details mesh (c) Near wall grid

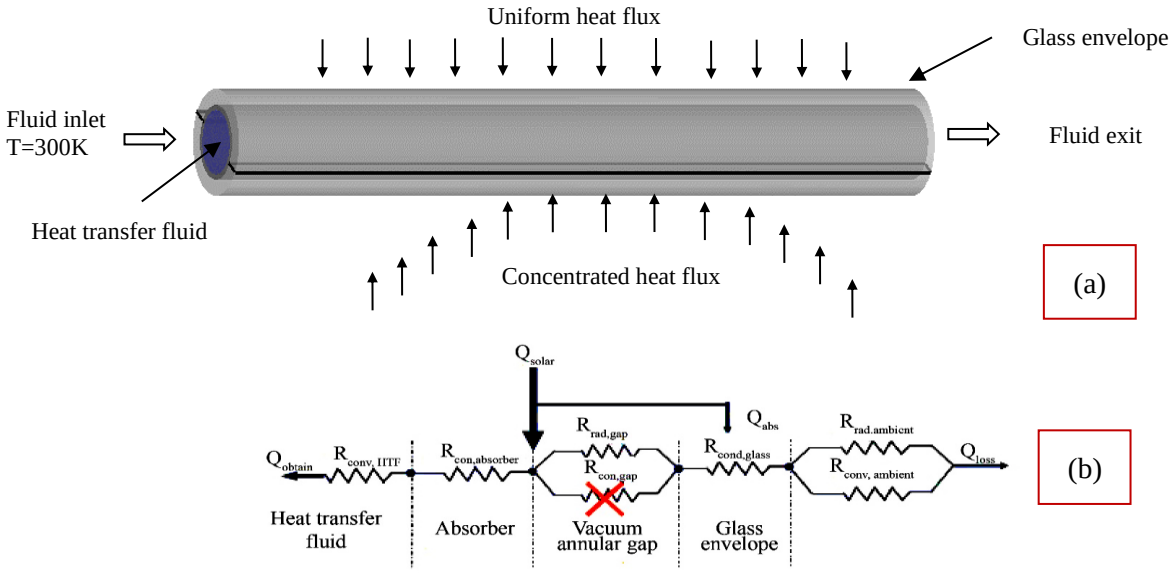

Fig. 9 A picture illustrating the receiver tube's structure: (a) Longitudinal view (b) Thermal connections of the PTC receiver

Heat balance on the absorber wall, which is applied to each HCE's control volume, is detailed in the following equation:

$$Q_{abs} = Q_u + Q_{loss} \quad (13)$$

Where:

$Q_{abs} = \alpha s.\ \tau.\ \rho.\ \gamma.\ A_a.\ G$

The formula used to quantify usable energy obtained from the HCE is as follows:

$$Q_u = \dot{m} C_p (T_s - T_{fi}) \quad (14)$$

The collector thermal heat losses may be determined in various ways, utilizing different reference temperatures in each case. The calculations for these losses are presented as follows:

$$Q_{loss} = Q_{loss(cv)} + Q_{loss(rd)} \quad (15)$$

$$Q_{loss(cv)} \approx 0$$

because annular space is under a vacuum $Q_{loss(rd)} = \frac{\sigma A_r (T^4{}_r - T^4{}_c)}{\frac{1}{\varepsilon_r} + \frac{1-\varepsilon_c}{\varepsilon_c}\frac{A_{ro}}{A_{ci}}} = \varepsilon_c A_{co} \sigma (T^4{}_c - T^4{}_{amb})$ (16)

The heat balancing equation is expressed as follows to each HCE's control volume:

$$Q_{abs} = Q_u + Q_{loss} \quad (17)$$

$$\alpha a.\tau.\rho.\gamma.Aa.G = \dot{m} C_p (T_s - T_{fi}) - \varepsilon_c A_r \sigma (T^4{}_c - T^4{}_{amb}) \quad (18)$$

$$\alpha a.\tau.\rho.\gamma.(Wa.L).G = \dot{m} C_p (T_s - T_{fi}) - \varepsilon_c (\pi d_o L) \sigma (T^4{}_c - T^4{}_{amb}) \quad (19)$$

$$(\pi d_o L)[\varepsilon_c \sigma (T^4{}_c - T^4{}_{amb})] = \alpha s.\tau.\rho.\gamma.(Wa.L).G + \dot{m} C_p (T_s - T_{fi}) \quad (20)$$

$$d_o = \frac{1}{\pi L} \frac{\alpha a.\tau.\rho.\gamma.(Wa.L).G - \dot{m} C_p (T_s - T_{fi})}{\varepsilon_c \sigma (T^4{}_c - T^4{}_{amb})} = \frac{\alpha a.\tau.\rho.\gamma.Wa.G}{\varepsilon_c \sigma (T^4{}_c - T^4{}_{amb})} + \frac{1}{\pi L} \frac{\dot{m} C_p (T_s - T_{fi})}{\varepsilon_c \sigma (T^4{}_c - T^4{}_{amb})} \quad (21)$$

$$d_o = \frac{1}{\varepsilon_c \sigma (T^4{}_c - T^4{}_{amb})} \left[\alpha a.\tau.\rho.\gamma.G.Wa + \frac{1}{\pi L} \dot{m} C_p (T_s - T_{fi})\right] \quad (22)$$

So, under steady-state conditions and for each control volume, temperatures remain constant and are determined using the FVM method. Hence, we can deduce this as a function of the optical characteristics of PTC and its dependence on W_a.

4.2.2. Optical Analysis

The Concentration Ratio (CR) is the primary factor that affects the reflector's optical efficiency and HCE in a PTC. The CR was expressed in Equation (3). For concentrators, CR is always greater than 1. In the case of a just one axis track collector, the maximum achievable concentration is determined by:

$$CR = \frac{1}{sin\theta_m} \quad (23)$$

θ_m : the half-acceptance angle.

5. Absorber Tube Diameter Optimization

5.1. Optical Results

Several numerical investigations of a PTC's receiver have been conducted using CFD models. The main emphasis is placed on examining the receiver tube diameter's influence on both the SHF and the heat transfer fluid, as stated by S. A. Murtuza et al. [22]. An investigation was conducted to examine how changing the diameter of an absorber affects the quantity of concentrated SHF reaching the periphery.

Comparing the SHF peaks for different absorber diameters indicates that increasing the absorber diameter results in a higher concentrated SHF on the absorber tube's exterior layer refer to Figure 10. Therefore, a large-diameter receiver is recommended. As previously stated, increasing the diameter of the receiver improves the PTC system's optical performance by boosting the SHF on its lower periphery. Consequently, it is intriguing to explore whether increasing the diameter of the absorber tube enhances the thermal efficiency of the PTC.

Accordingly, a CFD thermal analysis is conducted, and the outcomes are depicted in the upcoming section. According to the results obtained from the Soltrace software, it is evident that raising the absorber tube diameter brings about a higher SHF concentrated on the bottom side of the tube. Additionally, increasing the diameter of the tube results in a larger surface area exposed to the surroundings, which might contribute to higher heat losses to the outside. Consequently, it is intriguing to investigate whether the thermal effectiveness of the PTC system can be ameliorated for higher diameters or not.

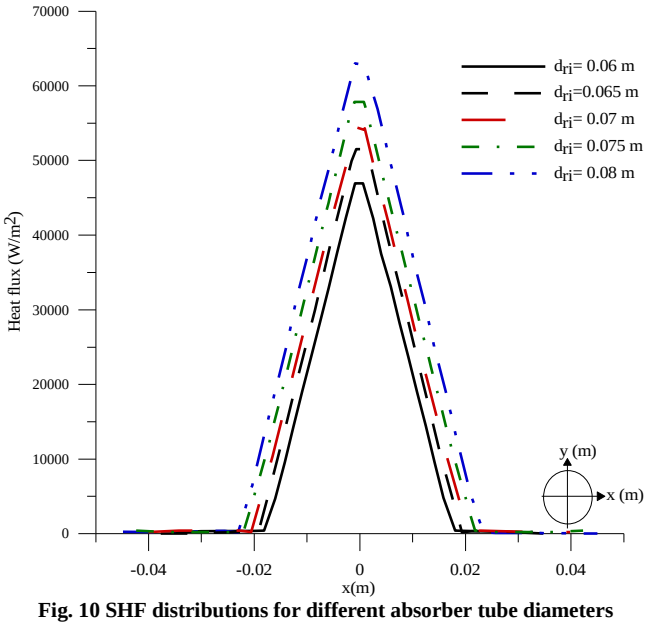

Fig. 10 SHF distributions for different absorber tube diameters

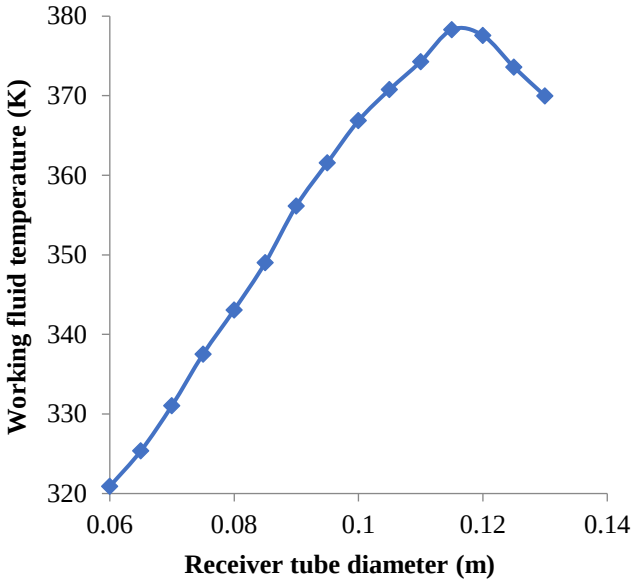

Fig. 11 Variation curve for heat transfer fluid outlet temperatures

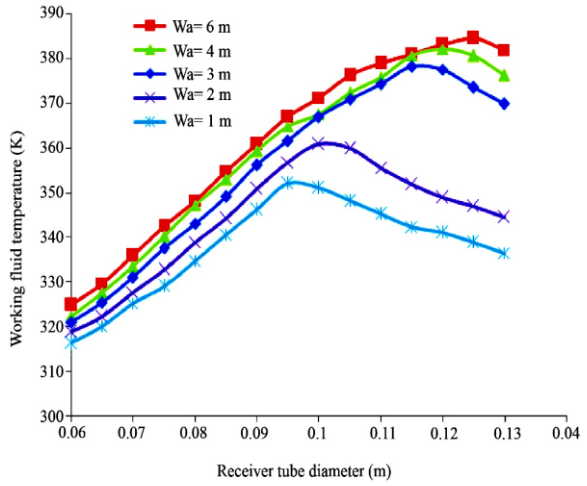

Fig. 12 Average outlet temperatures for diverse d_{ri} and for various W_a

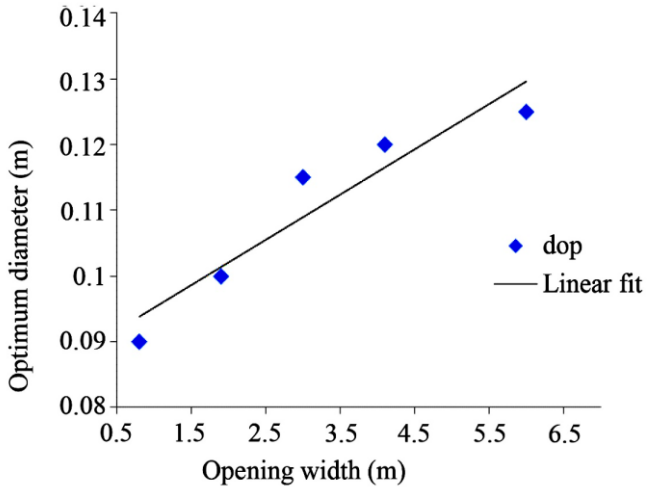

Fig. 13 The optimal diameters in relation to the opening widths W_a

5.2. Thermal Results

After examining the influence of the absorber tube diameter variation on the SHF, its effect on the thermal field is examined. Figure 11 depicts the heat transfer fluid temperatures' distributions for diverse absorber diameters. Increasing the diameter of the absorber results in a growth in SHF concentrated on the bottom of the absorber, thereby promoting a rise in the working fluid's outflow temperature. Figure 11 demonstrates a positive correlation between receiver diameter and the overage outflow temperature. However, there is undoubtedly an optimum diameter for the absorber tube (d_{ri} = 0,115 m), from which the temperature of the fluid falls at the exit section. It must not be denied that this optimal diameter is specific to the PTC configuration studied and detailed previously.

5.3. A New Generalized Correlation for the Optimum Diameter

In order to make a general statement about this discovery, a mathematical expression is formulated to ascertain the most favorable diameter for the absorber tube for any given size of the cylindro-parabolic reflector. This generalized expression, calculated using CFD simulations, simplifies the extraction of the optimal PTC receiver diameter for any PTC setup. In order to establish this correlation, several steps are adopted. Various configurations with several aperture widths (W_a) are tested, utilizing absorber tubes for different diameters. Soltrace software is used to evaluate the SHF distributions for varied aperture widths and various absorber tube diameters.

Afterwards, the SHF distribution in each scenario is imported into the ANSYS software as UDF coded in a C++ programme. Following this, a total of thirty-five CFD simulations are conducted. These simulations analyze the changes in fluid temperature for different receiver diameters and a wide range of aperture widths. The results of these simulations are presented in Figure 12. The optimal diameter of the tube for each configuration is subsequently calculated see Figure 12. The relationship between the optimum diameter (do) and the aperture width (Wa) is well-established and can be described by a linear trend, as shown in Figure 13. This allows us to derive a generalized expression for the optimum receiver diameter, which corresponds to the point where the performance of the PTC system starts to decline. It is established that the variation of optimum diameter (do) in the function of aperture width (Wa) follows a linear trend (see Figure 13), and it can be expressed as follows:

$$d_o = 0.006\ W_a + 0.088 \qquad (24)$$

This linear function precisely depicts the evolution of the optimal diameter for different opening widths. This new correlation is statistically significant with an R^2 =0.95. This universal expression will be beneficial and will be advantageous for every arrangement of the PTC system technology.

6. Conclusion

The investigation of the PTC's thermal performance commences by determining the distribution of concentrated SHF on the tube side that is exposed to the reflector, utilizing Soltrace software. The receiver tube's other side is directly exposed to sunlight, which is transmitted through the glass envelope. The SHF densities are utilized in a subsequent step by way of thermal boundary conditions on the receiver tube wall and simulated using ANSYS software.

Multiple receiver tube diameters were evaluated to identify the optimum diameter and the most effective one that enhances thermal performance. A new correlation has been developed, which has the ability to generalize this finding. At last, we are able to declare that the MCRT method, when linked with the CFD model, produces satisfactory outcomes. It has allowed the establishment of a general correlation that can determine the optimum and ideal diameter of the PTC receiver, regardless of the reflector dimensions.

Therefore, this finding eliminates the need for upcoming investigations to make experiments or numerical simulations to determine tube diameter for diverse reflector configurations, which could be truly useful in optimizing the PTC system's performance.

Acknowledgments

The authors express their gratitude to the members of the Higher Institute in Technology Study (ISET) of Tozeur, Tunisia, for their kind financial support of the research.

Nomenclature

General

a_λ = Spectral absorption coefficient
a = absorption coefficient
C_P = specific heat (J kg^{-1} K^{-1})
C_{pf} = working fluid specific heat (J kg^{-1} K^{-1})
d_{gi} = inner diameter of glass cover tube (m)
d_{go} = outer diameter of glass cover tube (m)
d_{ri} = inner diameter of absorber tube (m)
d_{ro} = outer diameter of absorber tube (m)
d_o = optimum diameter of absorber tube (m)
f = focal length (m)
g = gravity (g=9.801m s^{-2})
G = radiation intensity (W. m^{-2})
$G_{b\lambda}$ = The black body intensity, which is given by the Planck function
I = direct normal irradiance (DNI) (W m^{-2})
k = turbulent kinetic energy (m^2 s^{-2})
$\dot{m}$= mean mass flow rate (kg s^{-1})
N = refractive index
q = concentrated heat flux density (Wm^{-2})
q_a = average heat flux on whole tube surface (Wm^{-2})
$\vec{r}$ = position vector
$\vec{s}$ = direction vector
$\vec{s'}$ = diffusion vector
s = the path length
T = temperature (K)
T_{amb} = Ambient air temperature (K)
T_{fi} = inlet local fluid temperature
T_s = outlet temperature
T_c = glass envelope temperature
u, v, w = x, y, z velocity components (m s^{-1})
W_a = Aperture width (m)
V_w = wind velocity (m s^{-1})
x, y, z = Cartesian coordinates (m)

Greek symbols

σ_s = diffusion coefficient
σ = Steffan- Boltzman constant (5.672 x $10^{-8}Wm^{-2}K^{-4}$)
σ_{op} = optical error
σ_{slope} = slope error
σ_{spec} = specularity error
Φ = phase function
Ω' = solid angle
α_a = absorptivity of the absorber
β = thermal expansion coefficient (K^{-1})
ε = turbulent dissipation rate (m^2 s^{-3})
ε_c = envelope emissivity
τ = transmissivity
ρ = reflectivity
γ = intercept factor
η = efficiency (%)
κ = Von Karman constant= 0.42
λ = working fluid thermal conductivity (W m^{-1} K^{-1})
ν = working fluid viscosity (kg m^{-1} s^{-1})
ρ_0 = density at T_0 temperature (kg m^{-3})
φ = Rim angle (°)

Subscripts

CFD = computational fluid dynamics
C = concentration ratio
DO = discrete ordinate
FVM = finite-volume method
LCR = local concentration ratio
MCRT = Monte Carlo ray trace method
PTC = parabolic trough collector
RANS = Reynolds Averaged Navier Stokes
SHF = solar heat flux
HCE = heat collector element
HTF = heat transfer fluid

References

[1] Qianjun Mao, Yong Shuai, and Yuan Yuan, "Study on Radiation Flux of the Receiver with a Parabolic Solar Concentrator System," *Energy Conversion and Management*, vol. 84, pp. 1-6, 2014. [CrossRef] [Google Scholar] [Publisher Link]

[2] Aristotle T. Ubando et al., "Computational Fluid Dynamics on Solar Dish in a Concentrated Solar Power: A Bibliometric Review," *Solar*, vol. 2, no. 2, pp. 251-273, 2022. [CrossRef] [Google Scholar] [Publisher Link]
[3] Evangelos Bellos, Christos Tzivanidis, and Kimon A. Antonopoulos, "A Detailed Working Fluid Investigation for Solar Parabolic Trough Collectors," *Applied Thermal Engineering*, vol. 114, pp. 374-386, 2017. [CrossRef] [Google Scholar] [Publisher Link]
[4] Sheldon M. Jeter," "Calculation of the Concentrated Flux Density Distribution in Parabolic Trough Collectors by a Semi Finite Formulation," *Solar Energy*, vol. 37, no. 5, pp. 335-346, 1986. [CrossRef] [Google Scholar] [Publisher Link]
[5] Sheldon M. Jeter, "Analytical Determination of the Optical Performance of Practical Parabolic Tough Collectors from Design Data," *Solar Energy*, vol. 39, no. 1, pp. 11-21, 1987. [CrossRef] [Google Scholar] [Publisher Link]
[6] Z.D. Cheng, Y.L. He, and F.Q. Cui, "Numerical Study of Heat Transfer Enhancement by Unilateral Longitudinal Vortex Generators Inside Parabolic Trough Solar Receivers," *International Journal of Heat and Mass Transfer*, vol. 55, no. 21-22, pp. 5631-5641, 2012. [CrossRef] [Google Scholar] [Publisher Link]
[7] Dongqiang Lei et al., "An Experimental Study of Thermal Characterization of Parabolic Trough Receivers," *Energy Conversion and Management*, vol. 69, pp. 107-115, 2013. [CrossRef] [Google Scholar] [Publisher Link]
[8] M.D. Georgiou, A.M. Bonanos, and J.G. Georgiadis, "Optical Evaluation of Heliostat Mirrors Using Caustics," *Journal of Renewable and Sustainable Energy*, vol. 5, no. 5, 2013. [CrossRef] [Google Scholar] [Publisher Link]
[9] Marc Röger et al., "Techniques to Measure Solar Flux Density Distribution on Large-Scale Receivers," *ASME Journal of Solar Energy Engineering*, vol. 136, no. 3, pp. 1-10, 2014. [CrossRef] [Google Scholar] [Publisher Link]
[10] J. Delatorre et al., "Monte Carlo Advances and Concentrated Solar Applications," *Solar Energy*, vol. 103, pp. 653-681, 2014. [CrossRef] [Google Scholar] [Publisher Link]
[11] Zhuo Chen, Xinyue Han, and Yu Ma, "Performance Analysis of a Novel Direct Absorption Parabolic Trough Solar Collector with Combined Absorption using MCRT and FVM Coupled Method," *Renewable Energy*, vol. 220, 2024. [CrossRef] [Google Scholar] [Publisher Link]
[12] Fuqiang Wang et al., "Effects of Material Selection on the Thermal Stresses of Tube Receiver under Concentrated Solar Irradiation," *Material and Design*, vol. 33, pp. 284-291, 2012. [CrossRef] [Google Scholar] [Publisher Link]
[13] Fuqiang Wang et al., "Thermal Stress Analysis of Eccentric Tube Receiver Using Concentrated Solar Radiation," *Solar Energy*, vol. 84, no. 10, pp. 1809-1815, 2010. [CrossRef] [Google Scholar] [Publisher Link]
[14] Asaad Yasseen Al-Rabeeah, Istvan Seres, and Istvan Farkas, "Experimental Investigation of Parabolic Trough Solar Collector Thermal Efficiency Enhanced with Different Absorber Coatings," *International Journal of Thermofluids*, vol. 19, pp. 1-8, 2023. [CrossRef] [Google Scholar] [Publisher Link]
[15] Mohamed Chafie et al., "Experimental Investigation of Parabolic Trough Collector System under Tunisian Climate: Design, Manufacturing and Performance Assessment," *Applied Thermal Engineering*, vol. 101, pp. 273-283, 2016. [CrossRef] [Google Scholar] [Publisher Link]
[16] Tim Wendelin, Aron Dobos, and Allan Lewandowski, "*SolTrace: A Ray-Tracing Code for Complex Solar Optical Systems*," National Renewable Energy Lab, Technical Report, pp. 1-19, 2013. [CrossRef] [Google Scholar] [Publisher Link]
[17] *Ansys Fluent Theory Guide*, Ansys Inc, USA, pp. 724-746, 2013. [Google Scholar] [Publisher Link]
[18] National Renewable Energy Laboratory (U.S.), *Assessment of Parabolic Trough and Power Tower Solar Technology Cost and Performance Forecasts*, *National Renewable Energy Laboratory*, pp. 1-344, 2003. [Google Scholar] [Publisher Link]
[19] W.C. Swinbank, "Long-Wave Radiation from Clear Skies," *Quarterly Journal of the Royal Meteorological Society*, vol. 89, no. 381, pp. 339-348, 1963. [CrossRef] [Google Scholar] [Publisher Link]
[20] Soteris A. Kalogirou, "A Detailed Thermal Model of a Parabolic Trough Collector Receiver," *Energy*, vol. 48, no. 1, pp. 298-306, 2012. [CrossRef] [Google Scholar] [Publisher Link]
[21] Zhiyong Wu et al., "Three-Dimensional Numerical Study of Heat Transfer Characteristics of Parabolic Trough Receiver," *Applied Energy*, vol. 113, pp. 902-911, 2014. [CrossRef] [Google Scholar] [Publisher Link]
[22] Syed Ameen Murtuza et al., "Experimental and Simulation Studies of Parabolic Trough Collector Design for Obtaining Solar Energy," *Resource-Efficient Technologies*, vol. 3, no. 4, pp. 414-421, 2017. [CrossRef] [Google Scholar] [Publisher Link]
[23] S.C Mullick, and S.K. Nanda, "An Improved Technique for Computing the Heat Loss Factor of a Tubular Absorber," *Solar Energy*, vol. 42, no. 1, pp. 1-7, 1989. [CrossRef] [Google Scholar] [Publisher Link]
[24] Prashant Saini, Atul Dhar, and Satvasheel Powar, "Performance Evaluation of a Parabolic Trough Collector with a Uniform Helical Wire Coil Flow Insert," *Results in Engineering*, vol. 21, pp. 1-17, 2024. [CrossRef] [Google Scholar] [Publisher Link]
[25] Tawfiq Chekifi, and Moustafa Boukraa, "Thermal Efficiency Enhancement of Parabolic Trough Collectors: A Review," *Journal of Thermal Analysis and Calorimetry*, vol. 147, pp. 10923-10942, 2022. [CrossRef] [Google Scholar] [Publisher Link]